Design and Optimization of Adaptive Wings for Highly Efficient Long-Range Aircraft

Tobias F. Wunderlich and Sascha Dähne

DLR, German Aerospace Center, 38108 Braunschweig, Germany

In order to investigate the potential of adaptive wing technology to reduce fuel consumption, two highly efficient long-range transport aircraft were designed. The first design is based on basic maneuver load alleviation and a conventional composite wing box structure and represents the reference aircraft. The second aircraft design introduces adaptive wing technology and advanced structural concepts to quantify the potential of active and passive load alleviation technologies. This paper presents the results of the aerostructural wing optimizations as an essential part of the design work. In the optimization process, high-fidelity simulation methods are used to determine the flight performance in transonic cruise flight and the loads in maneuver flight and to minimize the mass of the composite wing box in a structural sizing. Static aeroelastic effects are considered in all flight conditions. The minimization of fuel consumption for three typical flight missions represents the objective function. The design parameters describe the wing shape and the deflections of the control surfaces. Realistic constraints for the integration of the landing gear, engine nacelle and control surfaces are considered. The comparison of the two aircraft designs shows a potential for improving fuel efficiency by 5.4 %**.**

Nomenclature

A	aspect ratio
b	wingspan
c, c_{MAC}	chord, mean aerodynamic chord
g	acceleration of gravity
H	altitude
Ma	Mach number
$n = L/(m\,g)$	load factor
$R = \sum R_i$	range (sum of mission segment ranges)
S	wing area
$t, t/c$	airfoil and relative airfoil thickness
V	flight velocity
x, y, z	coordinates
α	angle of attack
δ	angle of control surface deflection
$\eta = 2y/b$	relative wingspan coordinate

Subscripts

CoG	center of gravity
CWB	center wing box
FS, MS, RS	front spar, middle spar, rear spar
HTP, VTP	horizontal tailplane, vertical tailplane
MG, NG	main gear, nose gear
SL	sea level
TAS	true airspeed
WBE	wing fuselage engine configuration

Abbreviations

CO_2	Carbon dioxide
CS	Certification Specifications
FAR	Federal Aviation Regulations
RANS	Reynolds-averaged Navier–Stokes

1 Introduction

The environmental impact and resource requirements of commercial aviation are increasing with the growth of global mobility and transportation. Aviation is undergoing a transformation process towards more energy-efficient air transportation in order to protect the environment and conserve resources. DLR's Aviation Research Strategy [1] describes and specifies the contribution of aeronautics research to achieve the goals of the mobility strategy of the European Green Deal [2]. The corresponding target for the vehicle is a 50 % reduction in the aircraft's energy requirements.

The efficiency of commercial aircraft is determined by aerodynamic performance in terms of the lift-to-drag ratio, the empty mass of the aircraft and the thrust-specific fuel consumption of the engine. In order to find the optimal trade-off between cruise performance and wing mass, the method of aerostructural wing optimization was developed,

which combines aerodynamic shape optimization and structural sizing of the wing box with an appropriate optimization algorithm. Thereby, the interaction of aerodynamic forces and wing deformations are considered to enable accurate prediction of flight performance and static maneuver loads using fluid-structure coupling. Improvements in automation and the coupling of accurate simulation methods lead to the emergence of multidisciplinary design optimization (MDO) based on high fidelity simulation methods. The challenge in using MDO based on high fidelity methods is the large number of design parameters and constraints and the increased computing effort. In order to overcome this issue, the adjoint method enables the efficient calculation of the flow variable gradients as a function of the design parameters for gradient-based optimization [3, 4]. Up-to-date applications of the adjoint approach for multidisciplinary wing optimization have been shown in the publications of Kenway and Martins [5]; Liem, Kenway and Martins [6]; Keye et al. [7] and Abu-Zurayk et al. [8]. These publications show that the gradient-based optimization using the adjoint approach is an adequate method for multidisciplinary wing optimization with high fidelity simulation programs and a large number of design parameters.

An alternative MDO approach has been used in this work, as gradients cannot be calculated efficiently for all relevant disciplines. This applies particularly to cases that involve CAD modeling and structural sizing of composite structures using proprietary codes. An optimization strategy for finding the global optimum is used here. In addition, a lot of practical constraints can be taken into account, such as the integration of the main landing gear, the arrangement of the engines under the wing and the space allocation for the control surfaces including their actuators . Neglecting the main landing gear integration leads to unrealistic optimization results as shown in [5].

Further improvements can be achieved by adapting the wing shape to the present flight condition. Adaptive wing technology has been summarized, for example, by Martins [9] under the synonym of morphing wing. Variable camber using trailing edge devices is the most promising type of wing morphing for practical implementation. The basic phenomena of variable camber, the corresponding wing design philosophy and system requirements, and the advantages of the new wing concept are described by Szodruch and Hilbig [10]. Aerostructural design optimization published by Burdette, Kenway, and Martins [11] shows a potential 1.7 % reduction in fuel consumption by using a 10 % deep continuous morphing trailing edge. Reckzeh [12] describes the wing movables concept of the Airbus A350 in service. This concept provides a functional integration of high-lift with load and cruise performance control. The potential for reducing fuel consumption by improving cruise performance has been investigated for a long-haul passenger aircraft in our own research [13]. A fuel burn reduction between 0.5 % and 1.7 % has been predicted depending on the flight mission.

The technology of active maneuer load alleviation (MLA) reduces the aerodynamic loads using trailing edge control surface deflections to adapt the lift distribution under maneuver flight conditions. This technology has been published by White [14] for example and successfully applied to the Lockheed L-1011 [15]. In modern airliners, the maneuver load alleviation functions are an integral part of the flight control system. In order to reduce the loads due to atmospheric disturbances in flight, active gust load alleviation systems have been developed. An overview of applications of active control technologies for gust load alleviation has been given by Regan and Jutte [16]. The active and passive load alleviation technologies have to be integrated into the sizing process of the aircraft structure and result in longer maintenance intervals and mass reductions. Passive load alleviation technologies use specifically designed wing geometries and stiffness characteristics to reduce the loads due to aeroelastic deformations.

With increasing knowledge of composite materials further mass reduction potentials can be exploited by better adaptation of fiber direction to internal loads, introduction of advanced structural concepts, and new manufacturing processes. In the design process of composite structures a damaged tolerance design allowable typically limits the permitted strain level. The dependency of the damage tolerance allowable from the ply share of the laminate has been investigated by Bogenfeld et al. [17]. Based on the results of these studies an allowable increase between 30 % and 50 % has been identified. The introduction of new structural concepts in terms of load share between skin and stiffeners (e.g. “stringer dominant design”) and ply share selection for an increased strain allowable results in a reduction of the wing box mass. Further mass reduction potential has been identified due to permit local buckling after limit load (“post-buckling”). In addition, the increased allowables lead to more flexible wing structures that increase passive load alleviation.

The potential of load alleviation technologies has been investigated by Handojo et al. [18] for example. In this work a reduction of the wing box mass up to 27 % could be achieved for a long-haul airliner with unchanged secondary masses and fixed wing planform. The interactions of maneuver load alleviation, gust load alleviation and aeroelastic tailoring of the composite wing box structure have been investigated by Binder et al. [19] on the basis of results of different aeroservoelastic optimizations. Thereby, the outer wing shape and the topology of the wing structure have not been optimized and the deflections of the spoilers and ailerons have been used for active maneuver and gust load alleviation. The results show that 95 % of the maximum achievable mass reduction of a generic long range transport aircraft configuration can be achieved with the combination of maneuver load alleviation and aeroelastic tailoring of the wing box structure. In the multidisciplinary wing optimizations published by Wunderlich et al. [20] a significant mass reduction of the optimized wing box has been obtained for wings with active maneuver load alleviation, resulting in a drop in fuel consumption of about 3 %. Thereby, the wings with active maneuver load alleviation results in optimized wing geometries with increased aspect ratio and reduced taper ratio.

For a complete quantification of the potential of load reduction technologies, the various phases of aircraft design (conceptual design, preliminary design and detailed design [21]) must be taken into account. The publications already presented remain limited to the associated design phase with their estimates of the potential for load reduction due to the methodology used.

This publication presents the results of the aerostructural wing optimization, which is embedded in an aircraft design process consisting of overall aircraft design, aerostructural wing optimization, aircraft system design, loads analysis and aeroelastic design and detailed structural design and sizing. In the overall aircraft design, the specifications for the more accurate disciplinary design methods are generated and their provided results are synthesized. In the aerostructural wing optimization presented here, the optimal wing geometry is determined with the objective of minimizing fuel consumption. In the subsequent design processes, the loads of the controlled aircraft are determined for the optimized wing geometry and structural sizing is performed on this basis. The results obtained in the subsequent design processes are not the subject of this publication. Advanced technologies for active and passive load reduction have been integrated at all levels of the aircraft design process and the results have been exchanged via appropriate interfaces. The potentials quantified are limited to the aerostructural wing optimization process and represent a significant contribution to the overall quantification of the full potential of load reduction technologies.

2 Aircraft design process

In the DLR project oLAF (optimal load-adaptive aircraft) the potential for increasing efficiency by the use of active load alleviation technologies has been investigated. In order to quantify this potential, a long haul airliner with today's industrial state of the art structure and load alleviation technologies has been designed as a reference aircraft. Subsequently, the optimal load-adaptive aircraft has been designed based on the identical top level aircraft requirements (TLARs) and with the same design process with extensive use of advanced load alleviation technologies.

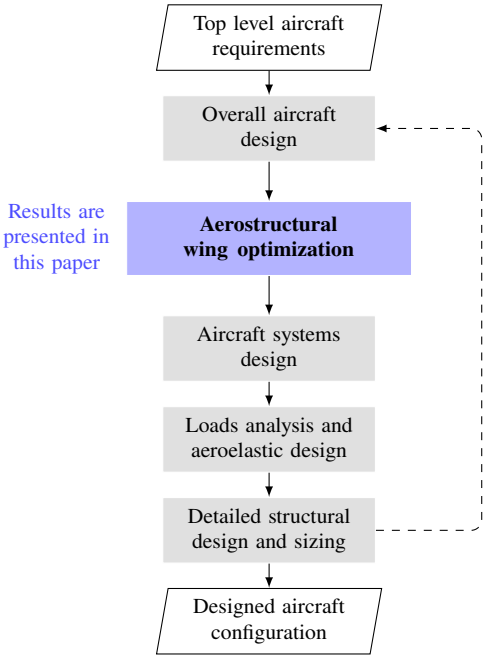

(a) Flow chart of the aircraft design process.

Design of the reference aircraft

- **Aerostructural wing optimizations**
  - **Twist and planform optimization**
  - **Twist and airfoil shape optimization**
- **Technologies used**
  - **State of the art maneuver load alleviation**
  - **State of the art strain allowable**
  - **Skin-dominated wing box design**

Design of the load-adaptive aircraft

- **Aerostructural wing optimizations**
  - **Twist optimization**
  - **Twist and planform optimization**
  - **Twist and control surface deflections optimization**
- **Technologies used**
  - **Adaptive wing**
  - **Extended maneuver load alleviation**
  - **Increased strain allowable**
  - **Stringer-dominated wing box design**
  - **Local buckling after limit load ("post-buckling")**

(b) Aerostructural wing optimizations and technologies.

Figure 1: Overview of the design process, aerostructural wing optimizations and used technologies.

Figure 1 shows the flow chart of the overall aircraft design process and the aerostructural wing optimizations performed for designing the reference aircraft and the load-adaptive aircraft. In addition, the used technologies are also listed. The design with state of the art maneuver load alleviation and structure technologies results in the reference aircraft. Based on advanced technologies, the load-adaptive aircraft is then designed using the same design process shown in Figure 1a.

The starting point of the design process are the TLARs, which have been defined for a highly efficient long-haul transport aircraft at the beginning of the project. With the overall aircraft design process the wing loading, thrust-to-weight ratio and the resulting aircraft size and masses have been estimated for the given transport task. Thereby, the transport task defines the flight missions in terms of payload, range and flight speeds.

Based on these results, an aerostructural wing optimization is executed to determine the optimal trade-off between aerodynamic cruise flight performance and wing mass. For the aerodynamic shape optimization, it was originally planned to use a separate three-dimensional gradient-based optimization process based on a high-fidelity simulation method under the consideration of airfoil thickness constraints. In the application of the design process, the aerodynamic shape optimization could be performed within the the aerostructural wing optimization process. The corresponding results are part of this publication.

Subsequent to the aerostructural wing optimization the aircraft systems design is executed. During the design of the aircraft systems, the architecture of the control surface actuation and flight control systems is determined, which also includes the implementation of load alleviation functions. The loads analysis and aeroelastic design process forms the next step in the design process. Within this process the aircraft loads are computed for the flight envelope. A detailed description of this process and the results of the first design iteration have been published by Schulze et al. [22]. As mentioned above, the individual processes are linked by manual interfaces with the support of the "Common Parametric Aircraft Configuration Schema" (CPACS) [23]. The result of the design process is the designed aircraft configuration after the iterative process has converged.

This paper presents the achieved results of the "aerostructural wing optimization" (blue box in Figure 1a) for the final design loop of the reference aircraft and the design optimizations of the load-adaptive aircraft. The design has been performed through several successive optimizations in order to investigate the influence of the individual technology steps and due to the limited number of design parameters of the selected global optimization strategy.

The next section describes the corresponding aerostructural wing optimization process and in Section 4 the technologies used for the load-adaptive aircraft are introduced. Section 5 shows the results of the multi-mission aerostructural wing optimizations. This includes the description of the design task and the baseline aircraft, the results of the twist and airfoil optimization resulting in the reference aircraft and the optimizations of the adaptive wing with advanced structure finally resulting in the load-adaptive aircraft.

3 Aerostructural wing optimization process

An integrated process chain for aerostructural wing optimization based on high fidelity simulation methods has been used for the presented optimizations of the twist distribution, the airfoil shapes, the wing planform and the control surface deflections. A detailed description of the original process chain and their successful application has been published by Wunderlich et al. [24]. The process chain include a mesh deformation techniques for geometry changes and simplified control surface deflections, a landing gear integration, a tail sizing based on handbook methods and a trim drag estimation functionality. The improvements described in the current article relate to the introduction of a component based fluid structure interaction, which allows the accurate consideration of wing deformations in the presence of an engine nacelle. A detailed description of the original process chain is outlined in the publication of Wunderlich et al. [25] and only the top level is presented here again.

3.1 Process chain for aerostructural wing analysis

The process chain applied in the present work is shown in Figure 2 in the form of XDSM-diagrams (Extended Design Structure Matrix) [26]. In each optimization step, the aircraft description of the baseline configuration is updated according to the current values of the design parameters. The resulting aircraft description is transferred to the subsequent simulation programs using the "Common Parametric Aircraft Configuration Schema" (CPACS) [23].

In the next step the parametric CAD model is updated, the aerodynamic volume mesh is deformed, and the structural model is generated. The parametric CAD model has been built in the commercial software CATIA® V5, which enables accurate surface representation, and robust and time efficient geometry changes.

In the CFD volume mesh deformation process, the mesh representing the baseline configuration is deformed in parallel for all flight conditions. According to the control surface deflection to be generated, the displacement field of the surface mesh is computed for each flight condition. It is then transferred to the CFD volume mesh using the Elasticity Analogy (EA) mesh deformation method [27] available in the FlowSimulator [28] environment.

For the generation of the structural model the DLR in-house tool "Design Environment for thin-walled Lightweight Structures" (DELiS) [29] is used. Based on the central data format CPACS, DELiS automatically generates a consistent finite element mesh. The finite element model is made up of shells elements enriched with physical properties of the wing spars, ribs, and skin cells and finally exported for the commercial FE solver MSC Nastran™.

The fluid-structure coupling loop is marked with a rounded yellow box and the values of the design mission lift-to-drag ratio, the wing mass and the objective function value are evaluated for the convergence examination.

For all flight conditions the aerodynamic forces and coefficients are computed using RANS-based CFD simulations. The flow simulations are performed by using the DLR TAU-Code [30] which is integrated in the HPC framework FlowSimulator [31].

Based on the aerodynamic loads computed for the flight conditions considered, the wing-box structure is sized. Within the structural analysis and sizing process the disciplinary objective is to fulfill the structural constraints in terms of

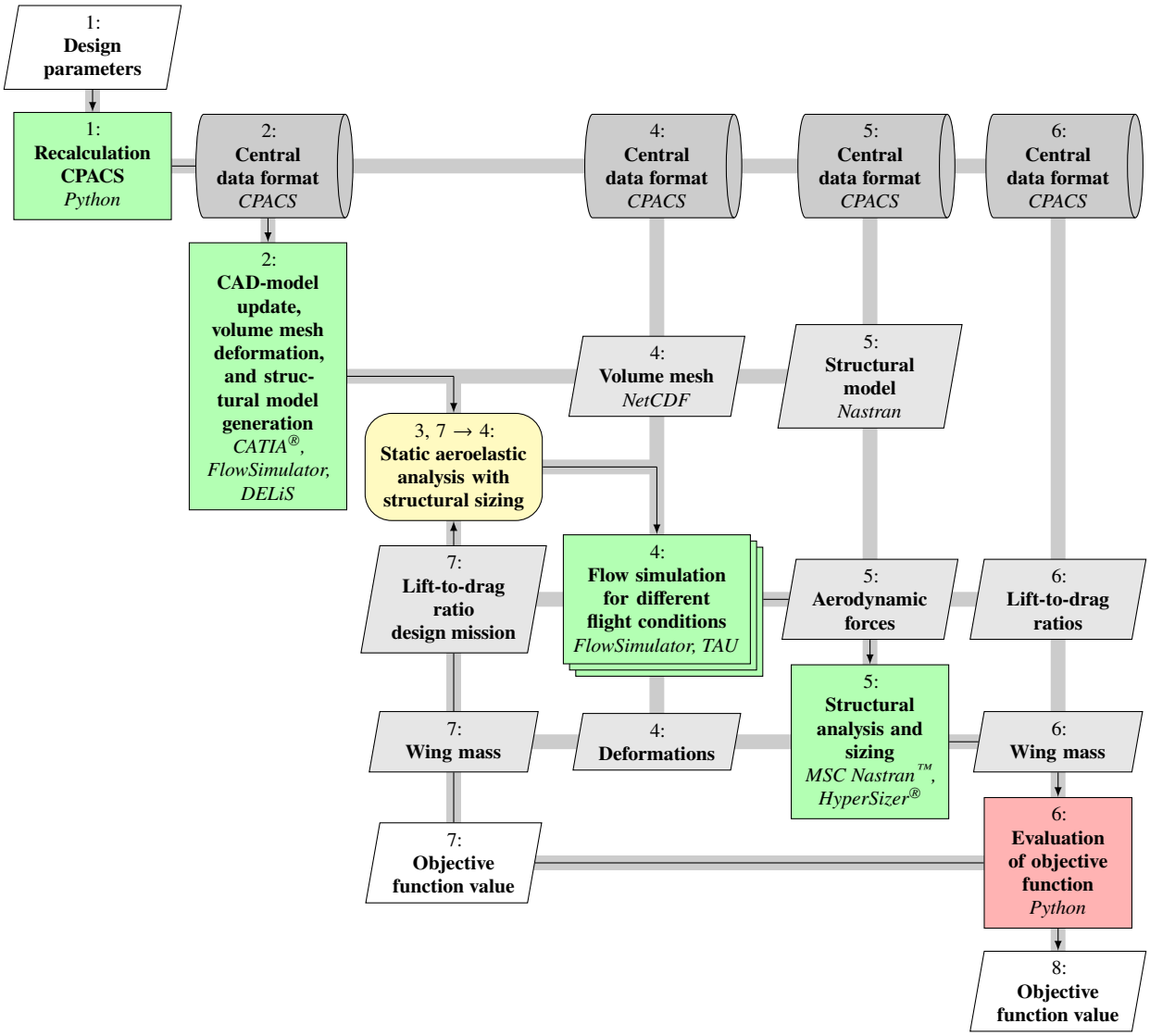

Figure 2: Flow chart of the process chain for aerostructural wing analysis.

failure criteria and converge the margins of safety (MoS) and wing mass. Hence, the structural analysis and sizing process represents a subspace optimization. Different design criteria are applied to ensure a valid structural design. As proposed by Dähne et al. [32] for stiffened panels, the criteria for strength, maximum strain, and local and global buckling are used for skin and all stringer components. The main results of this process are the wing mass and the deformed wing shapes for the flight conditions considered. The structural design process incorporates the commercial softwares MSC Nastran™ for computing internal loads and the commercial software HyperSizer® for application of design criteria in an automated and iterative fashion to size the composite wing box. The structural deformations form the input for the CFD volume mesh deformation. A mesh deformation method based on radial basis functions (RBF) [33] available in the FlowSimulator is used.

Afterwards, the objective function is evaluated and the convergence criteria of the static aeroelastic analysis are examined. Once convergence of the fluid-structure coupling loop is reached, the objective function value is given to the global optimizer.

3.2 Global optimization strategy

For the wing optimizations in this work an in-house surrogate-based optimization (SBO) method implemented by Wilke [34] has been selected. This global optimization strategy represents an adequate compromise between exploring the design space and locating the optimum. The selected optimization method is an implementation of the optimization method EGO (Efficient Global Optimizer), which has been introduced by Jones et al. [35] and is discussed in Forrester et al. [36]. At the beginning of the optimization a design of experiments (DoE) for a selected number of samples is performed. For the calculated objective function value and for each selected constraint, a surrogate model based on

kriging [37] is built. These surrogate models are able to model the non-linear behaviour of the objective and constraints. Additionally, a statistical error estimation is included.

Based on the surrogate models of the objective function and constraints, a hybrid optimization strategy is used to find the optimum in terms of expected improvement (EI), which combines the predictions of objective function value and model error. The hybrid optimization strategy starts with a global optimization method and the localization of the optimum is improved by the application of a local optimization method. For the resulting global optimum in terms of expected improvement a recalculation with the physical model is performed. The result of this recalculation is then used to improve the surrogate models for the objective function value and constraints. The described optimization procedure is iterated until convergence is reached.

4 Technologies

This section presents the technologies introduced to design a load-adaptive aircraft in the oLAF project. These are the adaptive wing, the increased strain allowable and post-buckling. For the quantitative assessment of these technologies with regard to fuel efficiency, the reference aircraft and the load-adaptive aircraft have been optimized with the identical aerostructural process, objective function and constraints.

4.1 Adaptive wing

Adaptive wing technology describes the controlled adaptation of the wing shape to different flight conditions with the aim of improving cruising performance and reducing loads in order to reduce mass and increase passenger comfort.

In this work multi-functional control surfaces at the wing trailing edge have been integrated into the aircraft configuration to introduce variable camber technology. The potential of fuel burn reduction due to cruise flight performance improvement has been shown in the publication of Wunderlich and Siebert [13] for a long-haul passenger aircraft with identical top level aircraft requirements (TLARs). The selection of control surfaces for cruise flight performance improvements has been derived from the results of this previous work to overcome the practical limitations in the number of design parameters. In comparison to this previous work, the technology of active maneuver load alleviation by the usage of trailing edge control surfaces and the structural sizing of the wing box have been added.

The active maneuver load alleviation (MLA) reduces the aerodynamic loads using trailing edge control surface deflections to adapt the lift distribution under maneuver flight conditions. In a pull up maneuver for example, an inboard load shift can be achieved by increasing the lift in the inboard region with positive control surface deflections and decreasing the lift in the outboard wing region with negative control surface deflections. The result of the inboard load shift are reduced aerodynamic loads in terms of wing bending moment.

4.2 Increased strain allowable and post-buckling

The structural concept of the conventional composite design consists of classical wing covers ply share and T-stringers. State of the art values for the strain allowable have been selected. For the structural concept of increased strain allowable and post-buckling, the classic skin-dominated design of the covers has been replaced by a stringer-dominated design. The selected values of the strain allowable and the corresponding percentage ply share of the covers, spars and ribs based on the calculations of damaged tolerance design allowables published by Bogenfeld et al. [17]. Furthermore, the structural technology of post-buckling has been introduced, which permits local buckling after limit load.

In Table 1 the differences between the structural concepts of the conventional composite wing design and the design with increased strain allowable and post-buckling have been summarized. The definition of the corresponding wing box regions are shown in Figure 3. The selected ribs spacing results from the required man holes in the lower cover of the wing box for safety checks and maintenance.

Table 1: Structural concepts overview.

		Conventional composite design	Increased strain allowable and post-buckling
Structural concept of the covers		Skin-dominated	Stringer-dominated
Stringer type		T-stringer	T-stringer
Strain allowable	Tension	4500 µm/m	6100 µm/m
	Compression	3500 µm/m	4400 µm/m
	Shear	9000 µm/m	8800 µm/m
Local buckling		No local buckling	Local buckling after limit load ("post-buckling")
Ribs spacing Δs_{Rib}	Center wing	0.85 m	0.85 m
	Inboard wing	0.85 m	0.85 m
	Middle wing	0.75 m	0.75 m
	Outboard wing	0.75 m	0.75 m
	Wing tip	0.50 m	0.50 m
Percentage ply share 0°/±45°/90°	Covers center wing	70/20/10	20/70/10
	Covers inboard wing	40/50/10	20/70/10
	Covers middle wing	40/50/10	20/70/10
	Covers outboard wing	30/60/10	20/70/10
	Covers wing tip	30/60/10	20/70/10
	Spars	50/40/10	20/70/10
	Ribs	40/50/10	20/70/10
	Stringers	70/20/10	70/20/10

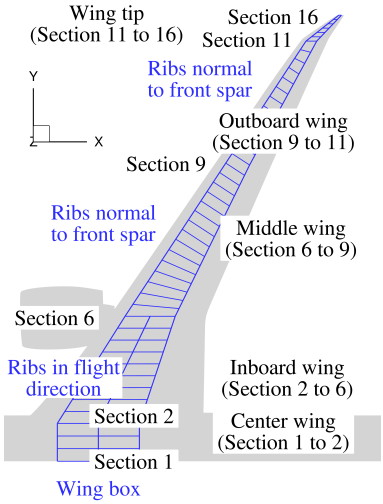

Figure 3: Wing box regions.

5 Aerostructural wing optimizations

For the design of the reference aircraft, multi-mission aerostructural wing optimizations have been successfully performed in order to optimize the wing planform, twist and thickness distribution of the baseline configuration. The baseline aircraft represents a conventional twin-engine wide-body configuration of a long-haul transport aircraft. The fuselage cross-section is elliptical and the wing is arranged as a low-wing aircraft. A new generation geared turbofan has been selected for the propulsion. The large engines are positioned under the wing and the main landing gear is attached to the wing.

In the first iteration loop, the shapes of the fuselage and the belly fairing have been designed. In addition, the external dimensions of the engine have been adapted to the engine design contributed by the DLR-Institute of Propulsion Technology. The introduced process for aerostructural wing optimization has been successfully applied to optimize the toe-in angle of the through-flow nacelle. The results of the first iteration loop are not presented here. In the second iteration loop, the aerostructural wing optimization has been repeated with the additional consideration of basic functions for maneuver load alleviation and of a touch-down maneuver load case in the structural sizing of the wing box. The results obtained form the baseline configuration.

The twist and airfoil optimization presented here leads to the final design of the reference aircraft, which represents the reference for the technology assessment. Based on the reference aircraft, the advanced technologies described in Section 4 have been introduced as a key difference in designing the load-adaptive aircraft. The results of the aerostructural wing optimizations are presented in Section 5 and the assessment of the adaptive wing and the advanced structural technologies is the content of Section 6.

5.1 Objective function, flight missions and load cases

The objective function of the multi-mission aerostructural wing optimizations is the combined fuel consumption per range and payload of three selected flight missions. Thus, the combined fuel consumption is the weighted sum of the fuel consumption of the corresponding missions as given in Equation (1).

$$\frac{m_F}{R\, m_P} = \sum_i w_i \left(\frac{m_F}{R\, m_P} \right)_i \tag{1}$$

Table 2 provides an overview of the selected flight missions and weighting factors. The specified flight envelope with the corresponding flight points is shown in Figure 4. With the selected weighting factors, the expected relative frequency of the missions in airline operation has been taken into account.

For the study and design mission the design Mach number of the Airbus A330 has been selected. The design mission take-off mass equals the maximum take-off mass and the range is set to 6000 nm. The corresponding payload results

Table 2: Flight missions and flight load cases.

Flight mission		Study mission	High-speed mission	Design mission
Weighting factor	w_i	0.6	0.1	0.3
Mach number	Ma	0.83	0.85	0.83
Range	R	4000 nm 7408 km	4000 nm 7408 km	6000 nm 11 112 km
Payload	m_P	40 800 kg	40 800 kg	-
Reserve fuel ratio	$m_{F,res}/m_F$	0.1400	0.1400	0.1000
Flight load case		**Pull up maneuver**	**Push over maneuver**	**Roll maneuver**
Altitude	H	0 m	3048 m	0 m
Mach number	Ma	0.552	0.655	0.552
Lift coefficient	C_L	0.744	−0.305	0.593
Load factor	n	2.5	−1.0	2.0

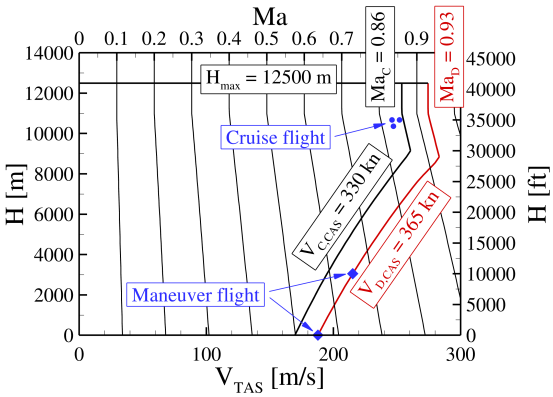

Figure 4: Flight envelope.

from the aerostructural wing analysis, which provides the required mission fuel and wing mass. The selection of range and payload for the study mission is based on a typical long-haul mission with a passenger load factor of 0.85 and represents the mission for which the aircraft will be optimized primarily. The difference between high-speed and the study mission is the increased cruise Mach number to consider off-design conditions in the wing optimization.

For the structural sizing of the wing box the maneuver load cases with the maximum loads have to be defined. These maneuver load cases have been derived from the flight envelope in Figure 4 and the limits of the maneuvering load factor resulting from the certification regulations CS-25/FAR 25. In Table 2 an overview of the selected maneuver load cases is given. The longitudinal trim of the aircraft for the given center of gravity position is taken into account for all maneuver load cases. In addition to the presented maneuver flight load cases a touch down load case has been introduced to consider the landing gear loads in the wing box sizing.

A conceptual design model has been used to calculate the fuel consumption of the individual flight missions. In this model, the cruise segment of the mission is described by the well-known Breguet range equation. The thrust-specific fuel consumption has been derived from the engine map of the geared turbofan provided by the DLR-Institute of Propulsion Technology. The lift-to-drag ratio in cruise is obtained from the aerodynamic coefficients of the flow simulation for the wing-fuselage-engine configuration, the estimated aerodynamic coefficients of the tailplane and the specified residual drag and residual thrust coefficients. The longitudinal trim of the aircraft for the given center of gravity position is taken into account. Further details on the models and equations used are described by Wunderlich et al. [24].

5.2 Constraints

In the aerostructural wing optimizations, geometric constraints for the geometry of the wing box, the control surface extensions, the integration of the main landing gear and the installation of the engine nacelle under the wing were taken into account. Table 3 provides an overview of the constraints that have been taken into account. The geometric constraints used are described in more detail in Figure 5.

The fuselage shape and mass have been kept constant during the wing optimizations. In addition the maximum take-off mass, the maximum payload, and specific masses of the leading and trailing edges are constant. The wing mass is a result of the structural sizing of the wing box. During optimization, the required fuel tank volume is calculated for all selected flight missions and compared to the usable fuel tank volume. The aerodynamic coefficients in the aerodynamic simulation are corrected with a constant residual drag coefficient to account for drag from components that are neglected in the simulation, such as the engine pylon and flap track fairings. An additional residual thrust has been introduced to correct the coefficients in the simulation with a flow-through nacelle.

Table 3: Aircraft, wing and landing gear constraints.

Parameter	Value
Maximum take-off mass	m_{MTO} = 220 000 kg
Maximum payload	$m_{P,max}$ = 54 000 kg
Residual mass ratio	m_{Res}/m_{MTO} = 0.3952
Specific mass of leading edge	m_{LE}/S_{LE} = 30 kg/m^2
Specific mass of trailing edge	m_{TE}/S_{TE} = 50 kg/m^2
Wingspan (FAA Group V and ICAO Code E)	52 m $\leq b \leq$ 65 m
Fuel tank volume	$V_F \geq V_{F,req}$
Main gear wheel span (ICAO Code E)	9 m $\leq 2\, y_{MG} \leq$ 14 m
Nose gear static load ratio	5 % $\leq F_{NG}/mg \leq$ 20 %
Tip back angle	$\tau_{TB} \geq 15°$
Overturn angle	$\tau_{OT} \leq 63°$
Tail down angle	$\alpha_{TD} \geq 11°$
Tail clearance	$h_{TC} \geq$ 0.25 m
Wing and engine clearance (with 7° bank angle)	$h_{WC},\ h_{EC} \geq$ 0.4 m
Castor angle of main gear leg	$83° \leq \tau_{Cas} \leq 90°$
Distance between main gear and rear spar	0.6 m $\leq \Delta s_{MG/RS} \leq$ 1.6 m
Distance between flap and support beam	$\Delta s_{Flap/SB} \geq$ 0.2 m
Distance between flap and rear spar	$\Delta s_{Flap/RS} \geq 0.065\, c_{MAC}$
Distance between aileron and rear spar	$\Delta s_{Ail/RS} \geq 0.04\, c_{MAC}$
Residual drag coefficient	$C_{D,res}$ = 0.0018
Residual thrust coefficient (through-flow nacelle)	$C_{T,res}$ = 0.0030
Center of gravity position	36 % c_{MAC}

ICAO = International Civil Aviation Organization

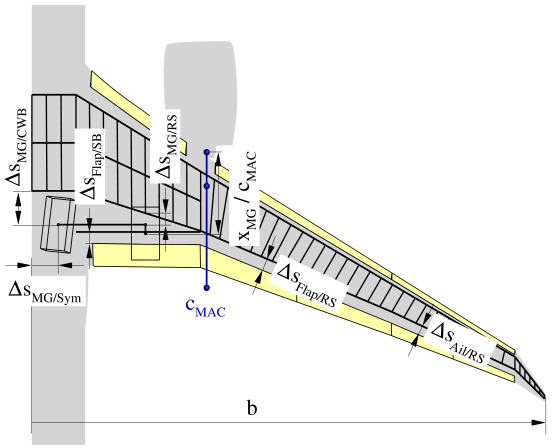

(a) Wing box and control surface extension constraints.

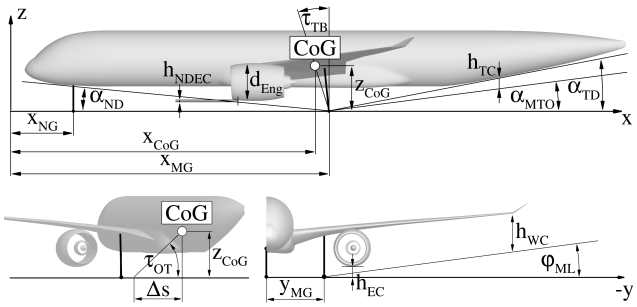

(b) Landing gear constraints.

Figure 5: Geometric constraints.

5.3 Baseline aircraft

The aerostructural wing optimizations shown here are based on a configuration, which was published by Wunderlich [38]. This configuration represents the baseline for the results presented here. The design of the baseline includes planform and twist distribution optimization and airfoil modifications to improve low-speed aerodynamic performance with identical objective function and constraints. The twist and airfoil optimization presented in the next section results in the reference aircraft for the technology assessment.

5.4 Reference aircraft - Twist and airfoil optimization

The optimal airfoil shapes of a given wing planform depend on the aerodynamic performance for design and off-design cruise conditions and the wing mass after structural sizing of the wing box. The design space for the airfoil shapes is limited by the requirements for low-speed performance with retracted high-lift devices.

The geometric modeling of the transonic airfoils is realized here using a parameterization method that enables continuous curvature of the airfoil shapes. The airfoil parameterization has the task of representing the design space of appropriate airfoil shapes with a minimum number of design parameters. In the leading edge region of the airfoil, a continuous curvature transition between the upper and lower surfaces must be ensured and the thickness of the trailing edge must be adjustable.

The “Class function/Shape function Transformation” (CST) method from Kulfan [39, 40] has been selected for the parameterization of the airfoils. In the classic CST method, Bernstein polynomials are used for the shape function. Due to the equidistant influence range of the Bernstein polynomials, a large number of parameters are required to resolve local details of the airfoil contour.

An extension of the CST method is therefore used here, which uses “Non-Uniform Rational Basis Spline” (NURBS) curves as shape functions. This extension allows to describe local details with a significantly smaller number of parameters. The CST method describes the upper side (index us) and the lower side (index ls) of the airfoil using the Equation (2) and (3).

$$\frac{z_{us}}{c} = C_{1.0}^{0.5}\, S_{us} + \left(\frac{z_{TE}}{c}\right)_{us} \frac{x}{c} \tag{2}$$

$$\frac{z_{ls}}{c} = C_{1.0}^{0.5}\, S_{ls} + \left(\frac{z_{TE}}{c}\right)_{ls} \frac{x}{c} \tag{3}$$

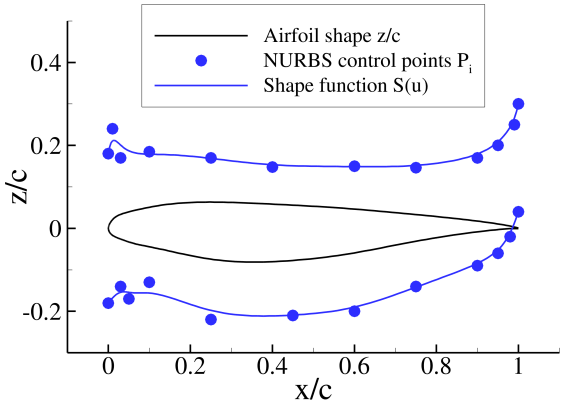

(a) CST parameterization with shape function based on "Non-Uniform Rational Basis Spline" (NURBS).

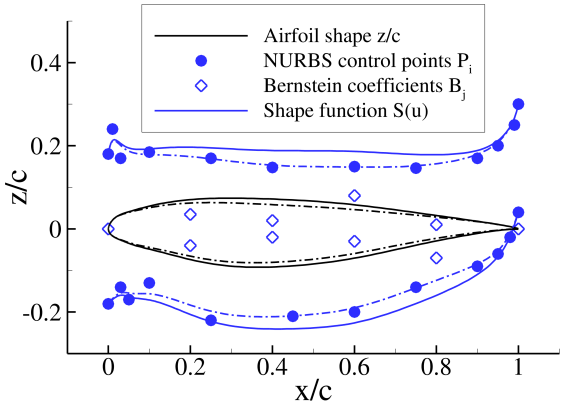

(b) CST parameterization with shape function variations based on Bernstein polynomials.

Figure 6: Airfoil parameterization based on extended CST method.

Table 4: Airfoil shape optimization design parameters.

Design parameter		Upper limit	Lower limit
Twist distribution	$\Delta\varepsilon_1$	−2.5°	0.5°
	$\Delta\varepsilon_6$	−1.5°	0.5°
	$\Delta\varepsilon_8$	−2.0°	0.5°
	$\Delta\varepsilon_9$	−2.0°	1.5°
	$\Delta\varepsilon_{11}$	−0.5°	2.5°
Bernstein polynomial coefficients section 3	$(B_{2,us})_3$	−0.05	0.05
	$(B_{3,us})_3$	−0.05	0.05
	$(B_{4,us})_3$	−0.05	0.05
	$(B_{2,ls})_3$	−0.10	0.20
	$(B_{3,ls})_3$	−0.10	0.20
	$(B_{4,ls})_3$	−0.20	0.10
Bernstein polynomial coefficients section 5	$(B_{2,us})_5$	−0.04	0.04
	$(B_{3,us})_5$	−0.04	0.04
	$(B_{4,us})_3$	−0.04	0.04
	$(B_{2,ls})_3$	−0.10	0.10
	$(B_{3,ls})_3$	−0.10	0.10
	$(B_{4,ls})_3$	−0.10	0.10
Bernstein polynomial coefficients section 7	$(B_{2,us})_7$	−0.03	0.03
	$(B_{3,us})_7$	−0.03	0.03
	$(B_{4,us})_7$	−0.03	0.03
	$(B_{2,ls})_7$	−0.06	0.06
	$(B_{3,ls})_7$	−0.06	0.06
	$(B_{4,ls})_7$	−0.06	0.06
Bernstein polynomial coefficients section 9	$(B_{2,us})_9$	−0.02	0.02
	$(B_{3,us})_9$	−0.02	0.02
	$(B_{4,us})_9$	−0.02	0.02
	$(B_{2,ls})_9$	−0.04	0.04
	$(B_{3,ls})_9$	−0.04	0.04
	$(B_{4,ls})_9$	−0.04	0.04

Here, $C_{1.0}^{0.5}$ is the so-called "Class Function". It is specified for profile geometries with a round nose and blunt trailing edge in Equation (4).

$$C_{1.0}^{0.5} = \left(\frac{x}{c}\right)^{0.5} \left(1 - \frac{x}{c}\right)^{1.0} \tag{4}$$

The expressions S_{us} and S_{ls} denoted by "Shape Function" describe the profile geometry. A distinction between the upper and lower side of the profile is not made in the following description in order to improve readability. The "Shape Function" used here consists of two parts according to Equation (5).

$$S(u) = S_{Bernstein}\left(\frac{x}{c}\right) + S_{NURBS,z}(u) \quad \text{with} \quad \frac{x}{c} = S_{NURBS,x}(u) \quad \text{for} \quad u \in [0,1] \tag{5}$$

The first part corresponds to the classic CST parameterization method of Kulfan [39, 40] with the use of Bernstein polynomials. This is extended here by a second part, which uses a NURBS curve. With this approach, both parts can be used independently according to their advantages and in combination. A description of the NURBS curves is not provided here and reference is made to the literature, e.g. by Piegl and Tiller [41].

Figure 6a shows an airfoil and the corresponding "Shape Function". The "Shape Function" is parameterized with 12 control points each for the upper and lower side of the airfoil using a B-spline curve of degree 4. With this relatively small number of parameters, the local details of the "Shape Function" in the the airfoil nose and trailing edge regions can be reproduced very accurately. Based on this precise description of the airfoil geometry, a geometry variation using the Bernstein polynomials is shown in Figure 6b. The Bernstein polynomial coefficients form the design parameters for optimizing the airfoil shape and are listed in Table 4. The selected values for the upper and lower limits guarantee feasible airfoil shapes and the required design space, which is aimed in particular at the front loading in the inboard wing region and the rear loading in the outboard wing region.

The result of the twist and airfoil optimization summarized in Table 5 shows a reduction in combined fuel consumption in the order of 3 %. This is due to an improvement in the lift-to-drag ratios under cruise conditions and a reduction in the

structural mass of the wing box by 6 %. The resulting twist and thickness distribution of the airfoil shape optimization is shown in Figure 7.

Table 5: Results overview of twist and airfoil optimization with conventional wing box structure.

Parameter	Variable	Baseline	Optimized airfoils	Difference
	Masses			
Mass of covers	$m_{W,covers}$	6524 kg	6734 kg	3.2 %
Mass of spars	$m_{W,spars}$	2866 kg	2306 kg	−19.5 %
Mass of ribs	$m_{W,ribs}$	2004 kg	1686 kg	−15.8 %
Wing box mass[a]	$m_{W,box}$	14 242 kg	13 408 kg	−5.9 %
Wing mass ratio	m_W/m_{MTO}	0.1034	0.0996	−3.7 %
Operational empty mass ratio	m_{OE}/m_{MTO}	0.5153	0.5115	−0.7 %
	Maneuver n = 2.5			
Control surface	$\delta_{Aileron,in}$	−10.0°	−10.0°	0.0 %
deflections	$\delta_{Aileron,out}$	−15.0°	−15.0°	0.0 %
Center of pressure	$y_{CoP}/(b/2)$	0.3401	0.3386	−0.4 %
	Study mission			
Lift-to-drag ratio	L/D	17.95	18.20	1.4 %
Center of pressure	$y_{CoP}/(b/2)$	0.3805	0.3777	−0.7 %
Fuel consumption	$m_F/(R\,m_P)$	1.4334×10^{-4} km^{-1}	1.4056×10^{-4} km^{-1}	−1.9 %
	High-speed mission			
Lift-to-drag ratio	L/D	17.20	17.23	0.2 %
Center of pressure	$y_{CoP}/(b/2)$	0.3796	0.3764	−0.8 %
Fuel consumption	$m_F/(R\,m_P)$	1.4847×10^{-4} km^{-1}	1.4735×10^{-4} km^{-1}	−0.8 %
	Design mission			
Payload	m_P	35 058 kg	36 597 kg	4.4 %
Used fuel tank volume ratio	$V_{F,req}/V_F$	0.7660	0.9010	17.6 %
Lift-to-drag ratio	L/D	18.08	18.31	1.3 %
Center of pressure	$y_{CoP}/(b/2)$	0.3788	0.3758	−0.8 %
Fuel consumption	$m_F/(R\,m_P)$	1.6704×10^{-4} km^{-1}	1.5845×10^{-4} km^{-1}	−5.1 %
	Objective			
Combined fuel consumption	$m_F/(R\,m_P)$	1.5096×10^{-4} km^{-1}	1.4661×10^{-4} km^{-1}	−2.9 %
CO_2 emissions per passenger kilometres[b]	$m_{CO2}/(R\,m_P)$	49.9 g_{CO2}/pkm	48.5 g_{CO2}/pkm	−2.9 %

[a] Values are scaled by a factor of 1.25 to account for additional masses of local reinforcements for load application and fasteners.
[b] Values of 3.15 kg_{CO2}/kg_{Fuel} for a turbofan engine [42] and 105 kg for the passenger mass with baggage are assumed.

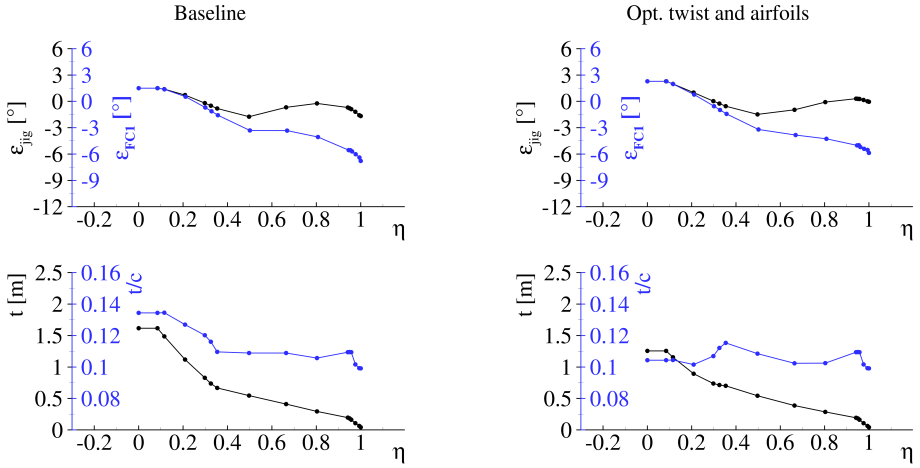

Figure 7: Twist and thickness distributions of twist and airfoil optimization with conventional wing box structure.

The aerodynamic improvements result from the curves of the isentropic Mach number shown in Figure 8 for the design Mach number of $Ma = 0.83$ and the off-design Mach number of $Ma = 0.85$. In the inner wing region (see curves in wing section 4), significantly more lift is generated in the front and middle region of the airfoil, so that the downforce on the horizontal tail required for trimming and the lift on the wing itself are reduced. This results in a reduction of the lift-dependent drag components. Furthermore, the curves of the isentropic Mach number in the middle wing region (see curves in wing section 8) show a significant reduction of the double shock system with the corresponding reduction of the wave drag. In the outer wing region (see curves in wing section 10) the Mach number was slightly reduced before the shock.

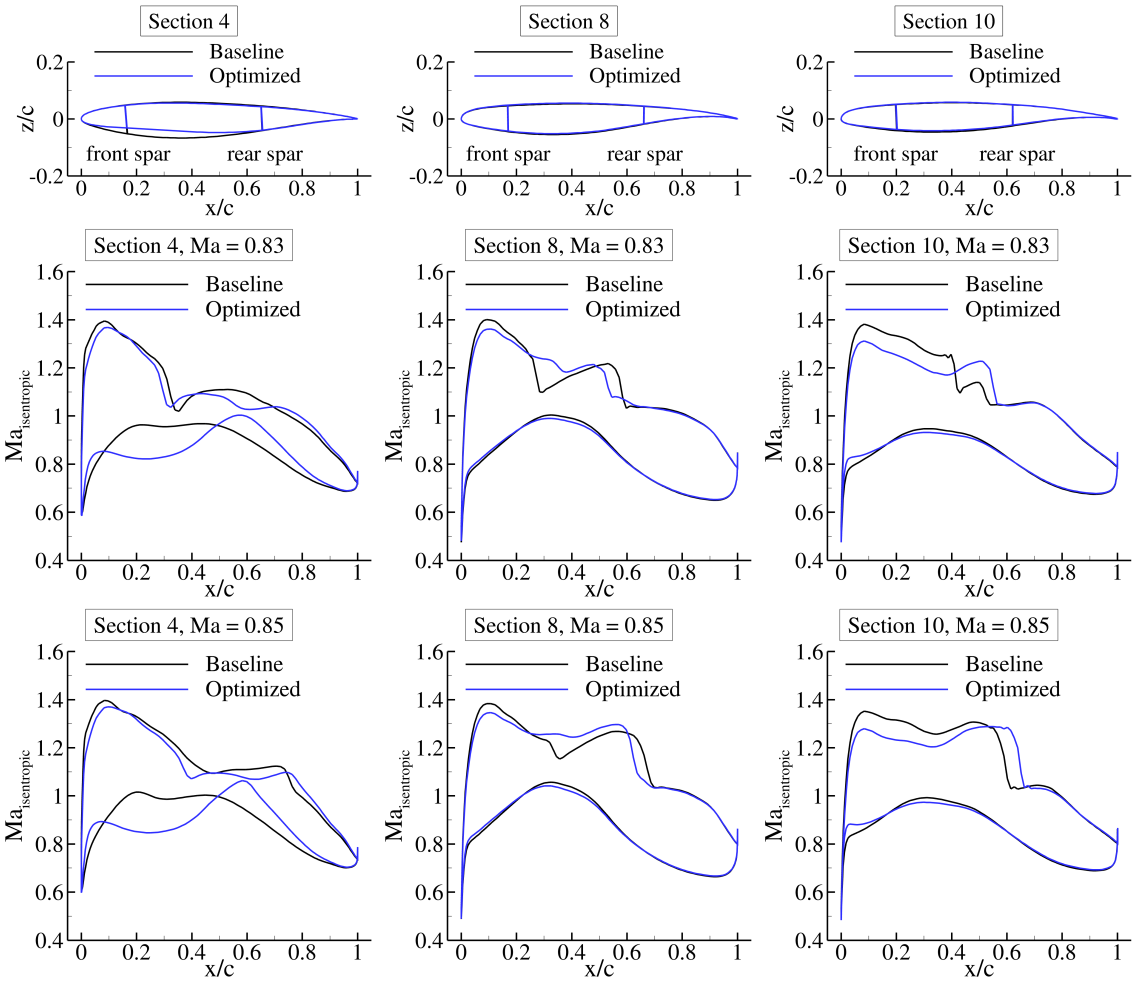

Figure 8: Airfoil shapes and isentropic Mach number distributions of twist and airfoil optimization with conventional wing box structure.

Although the thickness of the airfoil decreases in the inner wing region, the wing mass is reduced. A detailed evaluation of the component masses of the wing box in Table 5 shows the expected increase in the masses of the upper and lower covers, which in total leads to a mass reduction due to the significantly lower masses of the spars and ribs. Figure 8 contains the profile geometries in three wing sections resulting from the twist and airfoil optimization and Table 5 provides an overview of the optimization results.

5.5 Load-adaptive aircraft - Planform optimization of adaptive wing with advanced structure

The starting point for the planform optimization of the adaptive wing with advanced structure is the configuration with optimized airfoils from the previous section, which represents the reference aircraft. Based on this reference aircraft, the advanced structural concept with increased strain allowable and post-buckling described in Section 4.2 has been applied.

Due to the high number of design parameters, the wing optimization has been divided into three separate optimizations according to Table 6. The first optimization represents an optimization of the twist distribution of the wing with advanced structural concept in order to investigate the influence of this technology compared to the conventional composite design. In the next step, the wing planform is optimized taking into account the technologies of the adaptive wing described in Section 4.1. Here, the control surfaces on the trailing edge of the wing have been used for active maneuver load alleviation and cruise flight performance improvement. The corresponding control surface deflections for the different flight conditions have been prescribed (values are given in Table 7) and resulted from previously performed optimizations of the control surface deflections [13, 43], which are not the subject of this publication. In the last step, based on the results of the wing planform optimization, the twist distribution and the control surface deflections have been optimized in order to achieve the optimum of the adaptive wing with regard to minimizing fuel consumption. The final optimization result represents the load-adaptive aircraft. The definition of the design parameters used are shown in Figure 9 and Table 6 gives an overview of the design parameters of the three separate optimizations.

With each of the optimizations, fuel consumption has been further reduced, as shown in Table 7. With the introduction of the advanced structural concept and the optimization of the twist distribution, a significant reduction in the mass of

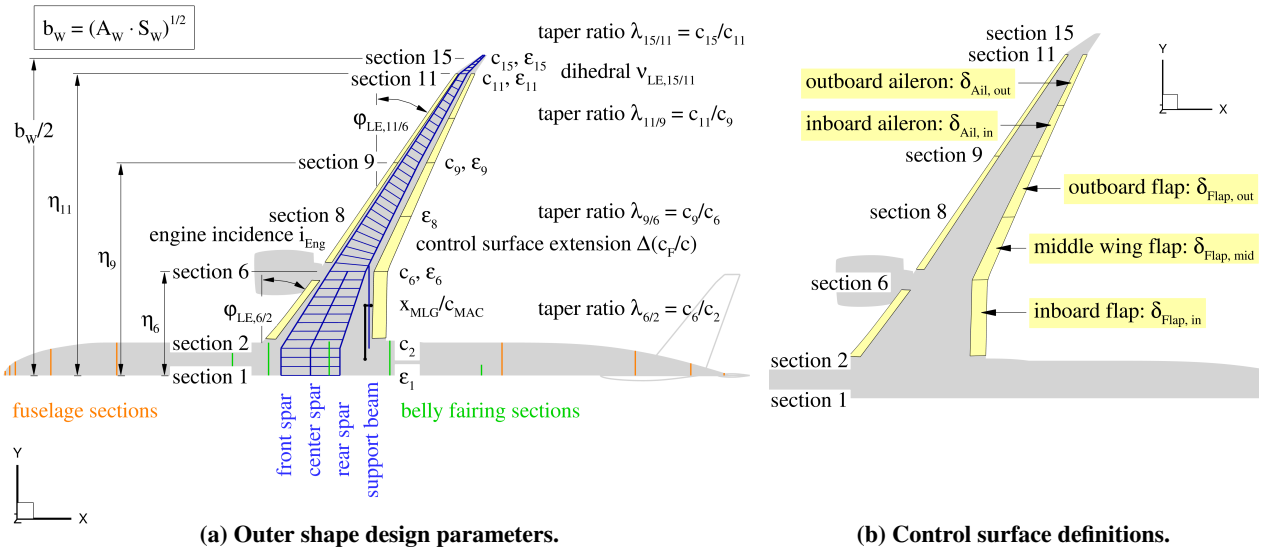

(a) Outer shape design parameters. **(b) Control surface definitions.**

Figure 9: Design parameters.

Table 6: Design parameters.

Parameter	Flight Case	Variable	Twist optimization	Planform optimization	Control surface deflections optimization
Wing area	-	S	-	1	-
Aspect ratio	-	A	-	1	-
Kink positions	-	$\eta_6,\ \eta_{11}$	-	2	-
Taper ratios	-	$\lambda_{6/2},\ \lambda_{9/6},\ \lambda_{11/9},\ \lambda_{15/11}$	-	4	-
Leading edge sweep angle	-	$\varphi_{LE,6/2},\ \varphi_{LE,11/6}$	-	2	-
Wing tip dihedral angle	-	$\nu_{LE,15/11}$	-	1	-
Twist distribution	-	$\varepsilon_1,\ \varepsilon_6,\ \varepsilon_8,\ \varepsilon_9,\ \varepsilon_{11},\ \varepsilon_{15}$	5	6	6
Control surface extension	-	$x_{TE,CS}/c$	-	1	-
Main landing gear position	-	x_{MG}/c_{MAC}	-	1	-
Engine angle of incident	-	i_{Eng}	-	-	1
Control surface deflections	FC1	$\delta_{Flap,in}$	-	-	1
	FC2	$\delta_{Flap,in},\ \delta_{Flap,mid},\ \delta_{Flap,out}$	-	-	3
	FC3	$\delta_{Flap,in}$	-	-	1
	LC1	$\delta_{Flap,in},\ \delta_{Ail,in},\ \delta_{Ail,out}$	-	-	3
	LC2	$\delta_{Flap,in},\ \delta_{Ail,in},\ \delta_{Ail,out}$	-	-	3
Number of design parameters		n_{DP}	5	19	18

the wing box in the order of 11 % and an improvement in the lift-to-drag ratios have been achieved in all cruise flight conditions considered. The improvement in the lift-to-drag ratios in cruise flight is due to the aerodynamically more favorable lift distribution, which represents the optimal compromise between flight performance in cruise flight and the maximum load in maneuver flight. Here, the significantly reduced wing mass leads to a shift of the optimal twist distribution to aerodynamically more favorable lift distributions. The reduced bending stiffness of the wing with the advanced structural concept also contributes to this wing mass reduction by increasing the passive load alleviation of the swept-back wing during maneuver flight. The outboard shift of lift is aerodynamically limited by an increase in the local lift coefficient at the outer wing and the corresponding non-linear increase in transonic wave drag.

Figure 10 and Figure 11 provide an overview of the geometries of the optimized wings. The results of the aerodynamic characteristics in cruise and maneuver flight are presented in the Figures 12, 13, 14 and 15. Figure 16 and Figure 17 show the internal loads of the optimized wings. The corresponding results of the structural sizing are given in Figure 18. Figure 19 shows the deformations of the optimized wings that occur during cruise and maneuver flight.

The optimization of the wing planform increases the lift-to-drag ratios under cruise flight conditions, while the increase in wing box mass is limited to 9.7 % by the introduction of adaptive wing technology. Figure 10 shows the optimized wing planform with the corresponding structural layout and the integration of the main landing gear. With the adaptive wing, the lift distribution in cruise flight has been shifted outboard as shown in Figure 12 to get a more favorable lift distribution in terms of induced drag. The corresponding center of lift is shown as a black circle. For each lift distribution, the related elliptical lift distribution is shown by a dashed line, and the corresponding center of lift is indicated by a gray square. The elliptical lift distribution is the optimum for planar wings in terms of lift induced drag.

Table 7: Results overview of wing optimizations with advanced wing box structure.

Parameter	Variable	Optimzed Twist	Optimized planform	Optimized planform and control surface deflections
		Masses		
Mass of covers	$m_{W,covers}$	5969 kg	6662 kg	6664 kg
Mass of spars	$m_{W,spars}$	1987 kg	2069 kg	2065 kg
Mass of ribs	$m_{W,ribs}$	1565 kg	1718 kg	1729 kg
Wing box mass[a]	$m_{W,box}$	11 900 kg	13 062 kg	13 074 kg
Wing mass ratio	m_W/m_{MTO}	0.0928	0.0980	0.0981
Operational empty mass ratio	m_{OE}/m_{MTO}	0.5047	0.5099	0.5099
		Maneuver n = 2.5		
Control surface deflections	$\delta_{Flap,in}$	0.0°	+15.0°	+15.2°
	$\delta_{Aileron,in}$	−10.0°	−12.5°	−12.0°
	$\delta_{Aileron,out}$	−15.0°	−20.0°	−20.0°
Center of pressure	$y_{CoP}/(b/2)$	0.3386	0.3072	0.3071
		Study mission		
Control surface deflections	$\delta_{Flap,in}$	0.0°	−2.5°	−2.6°
Lift-to-drag ratio	L/D	18.32	18.80	18.87
Center of pressure	$y_{CoP}/(b/2)$	0.3804	0.3801	0.3802
Fuel consumption	$m_F/(R\,m_P)$	1.3819×10^{-4} km^{-1}	1.3562×10^{-4} km^{-1}	1.3509×10^{-4} km^{-1}
		High-speed mission		
Control surface deflections	$\delta_{Flap,in}$	0.0°	−1.0°	−0.9°
	$\delta_{Flap,mid}$	0.0°	0.0°	+0.2°
	$\delta_{Flap,out}$	0.0°	+0.5°	+0.5°
Lift-to-drag ratio	L/D	17.37	17.85	17.88
Center of pressure	$y_{CoP}/(b/2)$	0.3790	0.3745	0.3740
Fuel consumption	$m_F/(R\,m_P)$	1.4473×10^{-4} km^{-1}	1.4169×10^{-4} km^{-1}	1.4147×10^{-4} km^{-1}
		Design mission		
Control surface deflections	$\delta_{Flap,in}$	0.0°	−1.5°	−1.7°
Payload	m_P	38 479 kg	38 670 kg	38 854 kg
Used fuel tank volume ratio	$V_{F,req}/V_F$	0.8946	0.9244	0.9218
Lift-to-drag ratio	L/D	18.45	18.91	18.98
Center of pressure	$y_{CoP}/(b/2)$	0.3781	0.3741	0.3744
Fuel consumption	$m_F/(R\,m_P)$	1.4986×10^{-4} km^{-1}	1.4631×10^{-4} km^{-1}	1.4520×10^{-4} km^{-1}
		Objective		
Combined fuel consumption	$m_F/(R\,m_P)$	1.4234×10^{-4} km^{-1}	1.3943×10^{-4} km^{-1}	1.3876×10^{-4} km^{-1}
CO_2 emissions per passenger kilometres[b]	$m_{CO2}/(R\,m_P)$	47.1 g_{CO2}/pkm	46.1 g_{CO2}/pkm	45.9 g_{CO2}/pkm

[a] Values are scaled by a factor of 1.25 to account for additional masses of local reinforcements for load application and fasteners.
[b] Values of 3.15 kg_{CO2}/kg_{Fuel} for a turbofan engine [42] and 105 kg for the passenger mass with baggage are assumed.

The additional usage of the inboard flap for active maneuver load alleviation shows a significant improvement in inboard load shift as shown in Figure 14.

Figure 13 presents the isentropic Mach number distributions for the upper wing surface of the optimized wings with advanced wing box structure for the study mission. The double shock system of the optimized twist configuration has been significantly improved by optimizing the wing planform and using the control surface deflections to optimize the lift distributions. The improvements in cruise performance in terms of lift-to-drag ratio result from the increased wingspan and the optimal compromise between induced and transonic wave drag.

Figure 14 shows the lift distributions for the maneuver flight with a load factor of $n = 2.5$, which determines the structural sizing due to the highest structural loads. The pronounced shift of the lift towards the inner wing becomes clear. This shift reduces the aerodynamic loads significantly and is due to the aeroelastic effects of the backward swept wing and the deflections of the control surfaces to reduce the load. By additionally using the inboard flap for load adaptation, the effect of load reduction has been further increased, which is indicated by the shift of the center of lift compared to the cruise flight position in Figure 12. During the maneuver flight with $n = 2.5$ no flow separation occurs, as the positive values of the skin friction coefficient distribution in Figure 15 show.

The optimized twist distributions of the configurations with adaptive wing technology in Figure 11 show greater differences between the twist angles in the unloaded state ("jig shape") in black compared to cruise flight in blue due to the increase in wing deformations shown in Figure 19. The differences in the wing deformations between the 1.0 g cruise flight and the 2.5 g maneuver flight are an indicator of how well the lift adaptation works through the use of optimized control surface deflections.

The corresponding internal loads in terms of shear force and bending moment have been analyzed for the loads reference axis defined in the Appendix. Figure 16 and Figure 17 shows the resulting internal shear force and bending moment distributions for the wing optimizations. The active and passive maneuver load alleviation of the adaptive wing

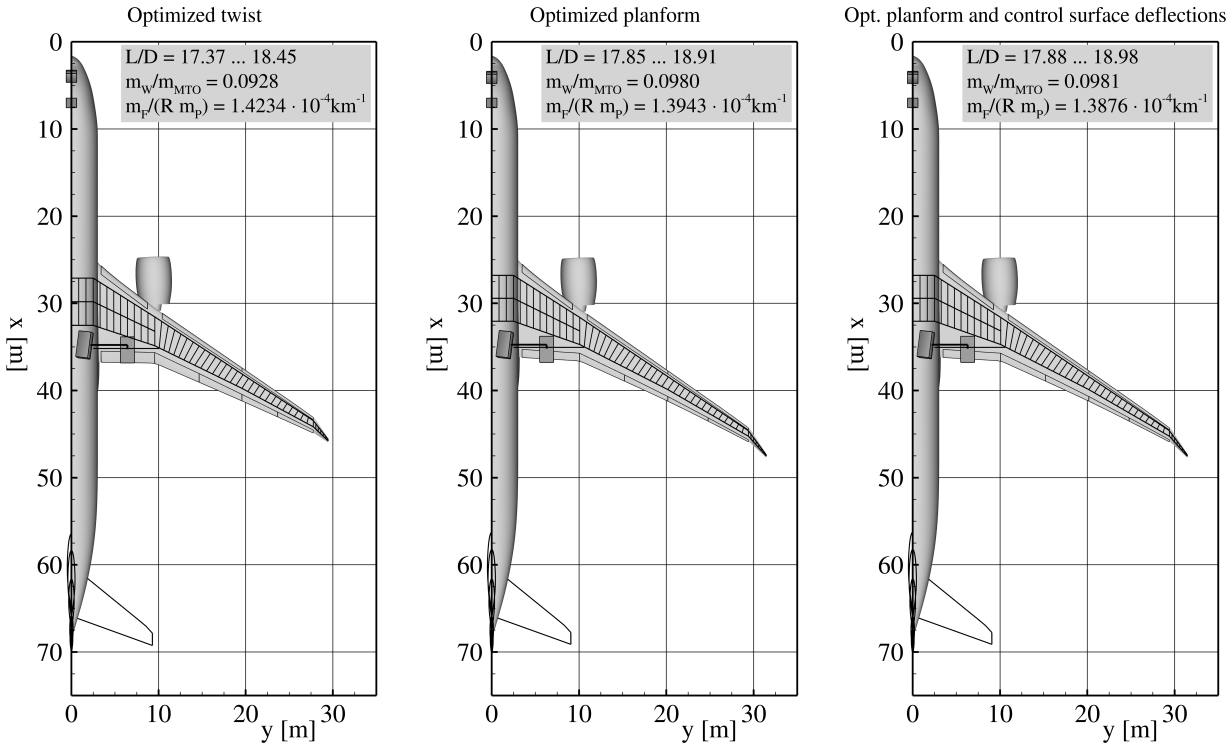

Figure 10: Wing planforms with structure layout of wing optimizations with advanced wing box structure.

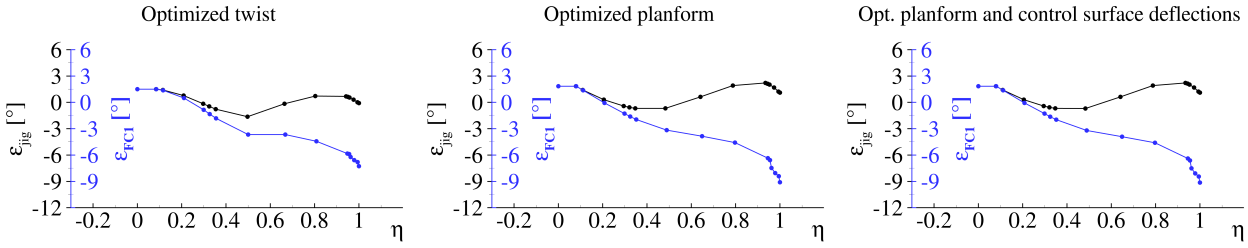

Figure 11: Twist distributions of wing optimizations with advanced wing box structure.

leads to a similar wing root bending moment in comparison to the wing with 13 % lower aspect ratio and state of the art maneuver load alleviation technology.

The resulting element thickness distributions are shown in Figure 18 for the optimized wings with advanced wing box structure. The corresponding mass breakdown of the wing box is given in Table 7. An increase in wingspan leads to an increase of the element thicknesses and the wing mass, which is strongly limited by the extended active maneuver load reduction of the adaptive wing with additional use of the inboard flap.

The final optimization of the control surface deflection angles shows slightly improvements in aerodynamic performance and a similar wing mass. The similar results in terms of control surface deflection angles indicate a suitable setting of the control surfaces in the planform optimization of the adaptive wing.

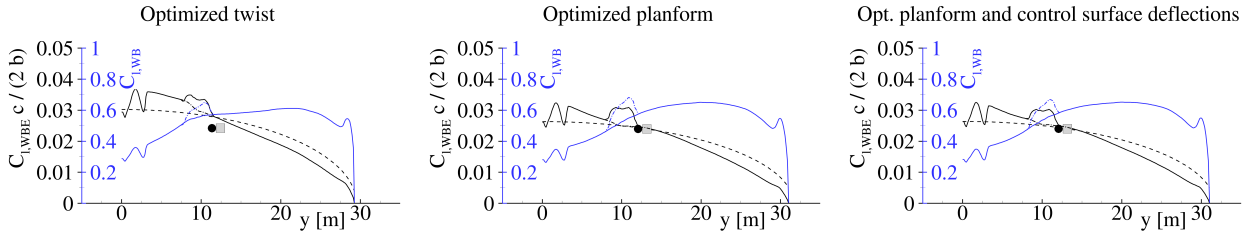

Figure 12: Lift and lift coefficient distributions for cruise flight of wing optimizations with advanced wing box structure (black circle: center of lift, gray square: center of lift for elliptical lift distribution).

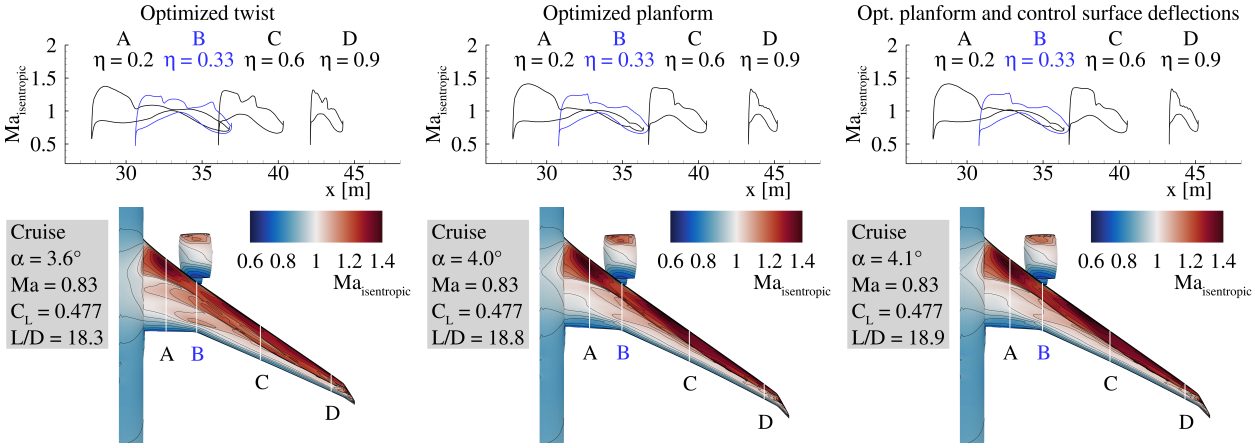

Figure 13: Isentropic Mach number distributions for upper wing surface of wing optimizations with advanced wing box structure.

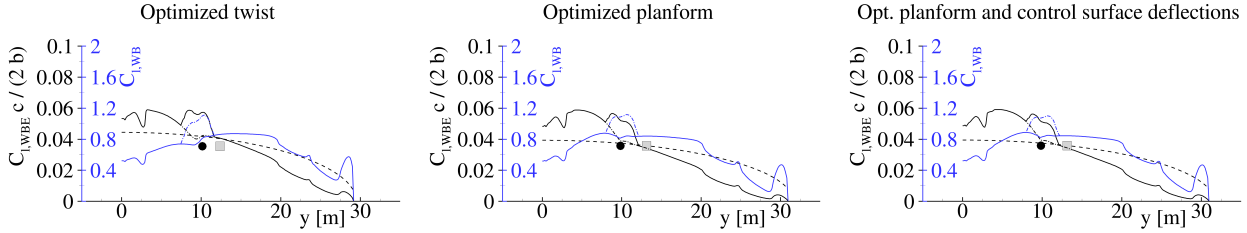

Figure 14: Lift and lift coefficient distributions for maneuver flight of wing optimizations with advanced wing box structure (black circle: center of lift, gray square: center of lift for elliptical lift distribution).

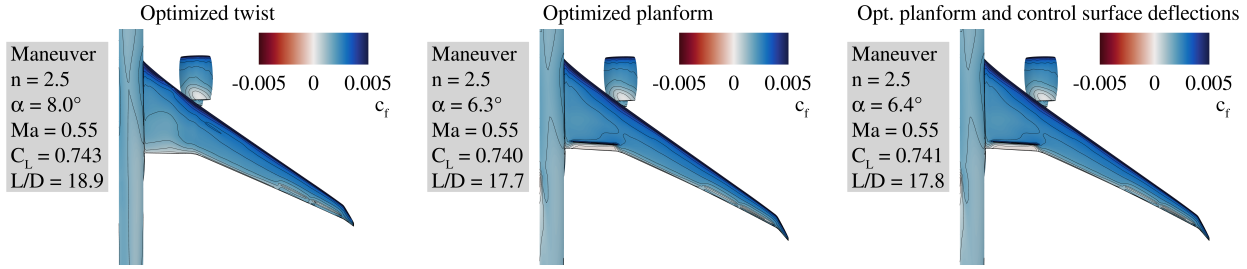

Figure 15: Skin friction distributions for maneuver flight of wing optimizations with advanced wing box structure.

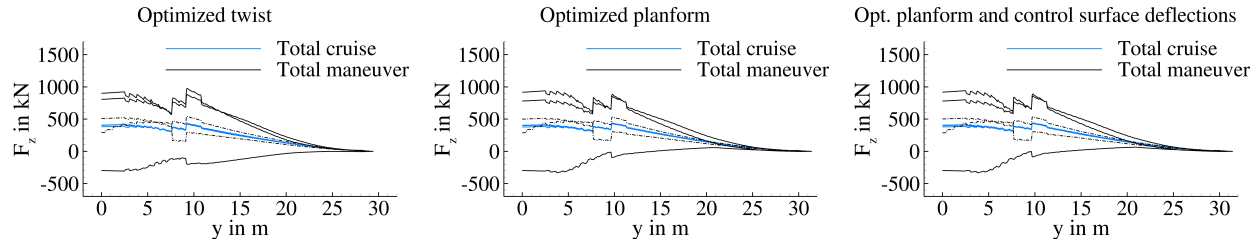

Figure 16: Internal shear force for cruise and maneuver flight of wing optimizations with advanced wing box structure.

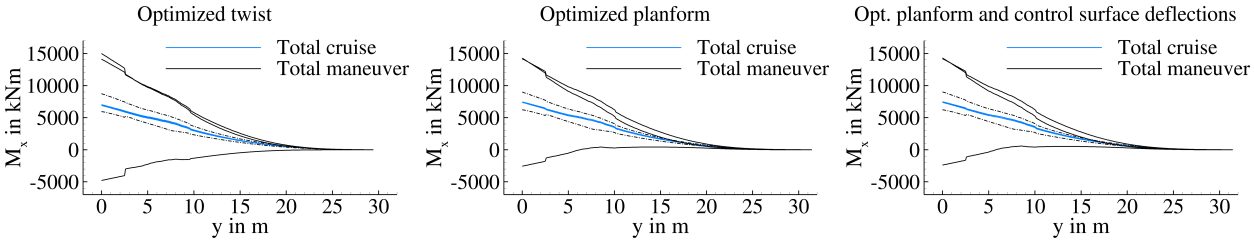

Figure 17: Internal bending moment for cruise and maneuver flight of wing optimizations with advanced wing box structure.

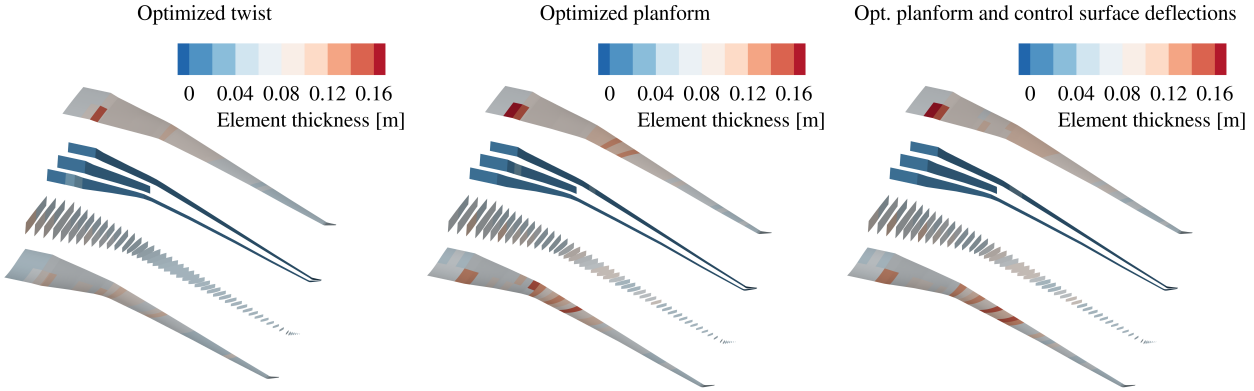

Figure 18: Wing box element thickness (skin thickness + stringer height) distributions of wing optimizations with advanced wing box structure.

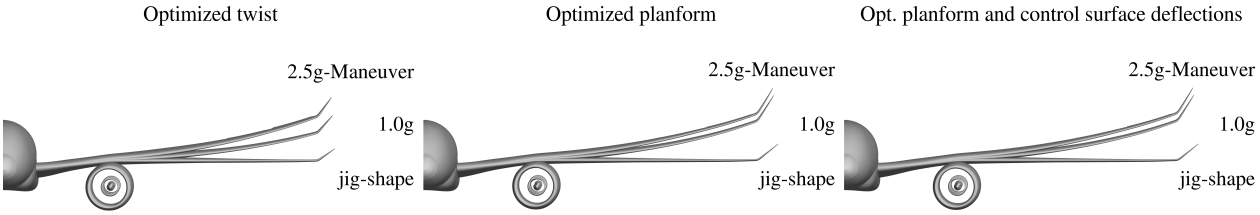

Figure 19: Wing deformations for cruise and maneuver flight of wing optimizations with advanced wing box structure.

6 Results overview and technology assessment

In Figure 20, an overview for the results of the aerostructural wing optimizations is shown. For all aerostructural wing analyses, the cruise lift-to-drag ratio, the wing mass ratio, and the corresponding combined fuel consumption are summarized. The results of the aerostructural airfoil shape optimization shows a fuel consumption reduction in tho order of 3 %. The integration of adaptive wing technology and advanced structural concept results in 3 % fuel efficiency improvement after twist distribution optimization for the same wing planform. The wing planform optimization shows a further potential of fuel saving in the order of 3 % due to the introduction of extended load alleviation and advanced structure technologies. The final optimization of the control surface deflections leads to a further fuel consumption reduction in the order of 0.5 %. In total a significant reduction of combined fuel consumption of 8.1 % in comparison to the baseline aircraft configuration [38] has been reached. The introduced technologies of adaptive wing and advanced wing structure with increased strain allowable and post-buckling show a potential of 5.4 % fuel efficiency improvement after aerostructural wing optimization. Table 8 summarizes the potential for reducing combined fuel consumption determined in the work presented.

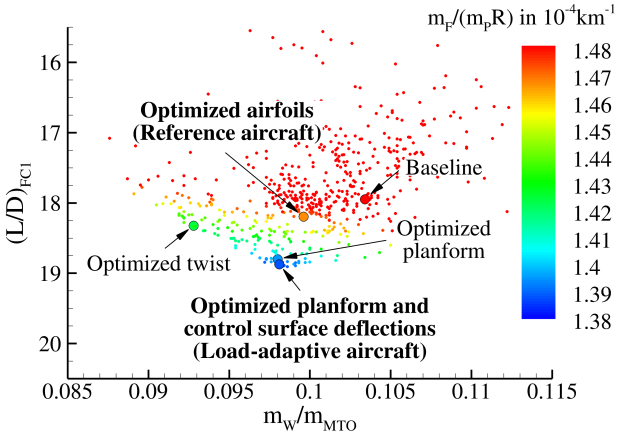

Figure 20: Aerostructural wing optimization results overview.

Table 8: Potential to reduce combined fuel consumption.

Optimization result	Reference	Reduction of combined fuel consumption
Optimized airfoils[a] (Reference aircraft)	Baseline[a]	2.9 %
Optimized twist[b]	Optimized airfoils[a] (Reference aircraft)	2.9 %
Optimized planform[b, c]	Optimized twist[b]	2.0 %
Opt. planform and control surface deflections[b, c] (Load-adaptive aircraft)	Optimized planform[b, c]	0.5 %
Opt. planform and control surface deflections[b, c] (Load-adaptive aircraft)	Optimized airfoils[a] (Reference aircraft)	5.4 %

[a] State of the art MLA and conventional composite wing box design
[b] Advanced structural concept with increased strain allowable and post-buckling
[c] Adaptive wing with variable camber and extended MLA

7 Conclusion and Outlook

In this work, the assessment of adaptive wing technology and the structural concept with increased strain allowable and post-buckling has been successfully demonstrated by using an integrated process for the aerostructural optimization of wings based on high fidelity simulation methods. The comparison of optimization results with the same objective function and the same constraints enables a realistic evaluation of these novel technologies. The constraints include the geometric constraints for the integration of the main landing gear, the engine nacelle and the control surfaces.

Airfoil optimization is a multidisciplinary task with the objective of finding the best compromise between aerodynamic performance in cruise flight and wing mass. The results obtained show optimal airfoil geometries with reduced airfoil thickness in the inner wing region, which showed a decrease in wing mass despite the expected increase in skin thickness of the covers.

The optimizations of the adaptive wing with advanced structural concept lead to optimal wing geometries with a higher span. Through the additional use of the flap in the inner wing region, the maximum internal loads could be

limited to values in the order of magnitude of the baseline wing with a smaller span. In the case of the backward swept wing, the load redistribution to the inner wing leads to a forward load shift, which causes additional fuselage loads due to the trim on the stabilizer. The corresponding effects on the structural sizing of the fuselage have been neglected. With the adaptive wing, the improvements in aerodynamic performance due to the lift shift towards the outer wing are limited by the trim and the wave drag. The adaptation of the wing shape to the current deformation due to mass changes during the flight mission becomes more important as the flexibility of the wing increases. The optimized wing geometries show a relatively high angle of attack in cruise flight, which can be explained by a reduction of the trim drag due to the pitching moment of the fuselage.

In the future, the engine design and the structural sizing of the fuselage structure have to be considered in the design optimization of the aircraft. Furthermore, with the increasing use of technology for active and passive maneuver load alleviation, the gust loads and technologies for their reduction must also be taken into account.

Appendix

7.1 Definition of the load reference axis

The internal loads presented in Section 5.5 have been analyzed for the loads reference axis defined in Figure 21. These internal loads are resulting from the external and inertial loads and in Figure 21 an example for the 2.5 g maneuver flight has been presented.

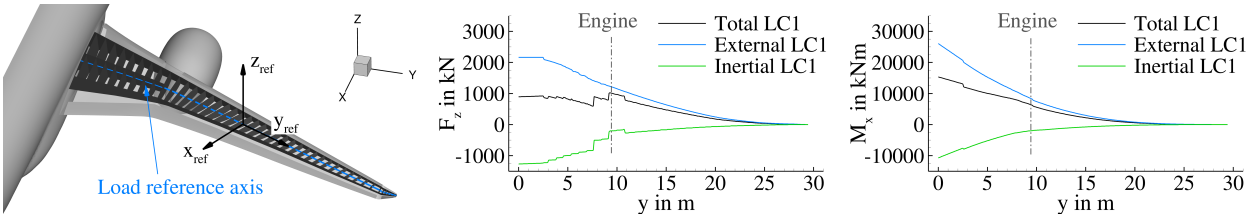

Figure 21: Definition of loads reference axis and example of internal loads for the maneuver flight with $n = 2.5$.

7.2 Additional results of the twist and airfoil optimization

The main results of the twist and airfoil optimization have been presented in Section 5.4 and additional results of the wing and tail geometry as well as the landing gear are given in Table 9.

Table 9: Additional results of twist and airfoil optimization with conventional wing box structure.

Parameter	Variable	Baseline	Optimized airfoils	Difference
	Wing geometry			
Wing area	S_W	337.004 m^2	336.995 m^2	−0.0 %
Wingspan	b_W	58.859 m	58.859 m	0.0 %
Mean aerodynamic chord	$c_{MAC,W}$	7.579 m	7.581 m	0.0 %
Aspect ratio	A_W	10.280	10.280	0.0 %
Taper ratio	λ_W	0.036	0.036	0.0 %
Leading edge sweep angle	$\varphi_{W,LE}$	34.5° to 39.6°	34.5° to 39.6°	0.0 %
Outboard dihedral angle	$\nu_{LE,11/6}$	5.0° to 5.5°	5.0° to 5.5°	0.0 %
Wing tip dihedral angle	$\nu_{LE,15/11}$	35.0°	35.0°	0.0 %
Flap spar offset	$\Delta s_{Flap/RS}$	0.607 m	0.607 m	0.0 %
Aileron spar offset	$\Delta s_{Ail/RS}$	0.311 m	0.310 m	−0.3 %
Useable fuel tank volume	V_F	116.804 m^3	98.338 m^3	−15.8 %
	Tail geometry			
Horizontal tail area	S_{HTP}	68.840 m^2	68.857 m^2	0.0 %
Vertical tail area	S_{VTP}	49.311 m^2	49.311 m^2	0.0 %
	Landing gear			
Landing gear wheel base	l_{LG}	28.349 m	28.349 m	0.0 %
Outer main gear wheel span	$2\,y_{MG}$	12.851 m	12.855 m	0.0 %
Nose gear static load factor	$F_{NG}/(m\,g)$	0.057 to 0.078	0.057 to 0.078	0.0 %
Tipback angle	τ_{tb}	18.0° to 24.6°	18.0° to 24.5°	−0.4 % to 0.0 %
Overturn angle	τ_{ot}	39.9° to 40.0°	40.0° to 40.1°	0.2 % to 0.3 %
Tail down angle	α_{TD}	11.1°	11.1°	0.0 %
Main gear spar offset	$\Delta s_{MG/RS}$	1.050 m	1.000 m	−4.8 %
Main gear flap offset	$\Delta s_{Flap/SB}$	0.282 m	0.281 m	−0.4 %

7.3 Additional results of the planform optimization of adptive wing with advanced structure

The main results of the planform optimization have been presented in Section 5.5 and additional results of the wing and tail geometry as well as the landing gear are given in Table 10.

Table 10: Additional results of wing optimizations with advanced wing box structure.

Parameter	Variable	**Optimzed Twist**	**Optimized planform**	**Optimized planform and control surface deflections**
		Wing geometry		
Wing area	S_W	337.3 m^2	334.6 m^2	334.6 m^2
Wingspan	b_W	58.89 m	62.85 m	62.85 m
Mean aerodynamic chord	$c_{MAC,W}$	7.58 m	7.27 m	7.27 m
Aspect ratio	A_W	10.283	11.806	11.806
Taper ratio	λ_W	0.036	0.033	0.033
Leading edge sweep angle	$\varphi_{W,LE}$	34.5° to 39.6°	35.1° to 39.3°	35.1° to 39.3°
Outboard dihedral angle	$\nu_{LE,11/6}$	0.0° to 1.0°	0.0° to 1.0°	0.0° to 1.0°
Wing tip dihedral angle	$\nu_{LE,15/11}$	35.0°	38.5°	38.5°
Flap spar offset	$\Delta s_{Flap/RS}$	0.61 m	0.69 m	0.69 m
Aileron spar offset	$\Delta s_{Ail/RS}$	0.31 m	0.34 m	0.34 m
Useable fuel tank volume	V_F	98.49 m^3	93.51 m^3	93.51 m^3
		Tail geometry		
Horizontal tail area	S_{HTP}	68.9 m^2	65.6 m^2	65.6 m^2
Vertical tail area	S_{VTP}	49.4 m^2	52.3 m^2	52.3 m^2
		Landing gear		
Landing gear wheel base	l_{LG}	28.33 m	28.27 m	28.27 m
Outer main gear wheel span	$2\,y_{MG}$	12.85 m	12.57 m	12.57 m
Nose gear static load factor	$F_{NG}/(m\,g)$	0.056 to 0.078	0.056 to 0.076	0.056 to 0.076
Tipback angle	τ_{TB}	17.2° to 23.6°	17.5° to 23.8°	17.5° to 23.8°
Overturn angle	τ_{OT}	41.0° to 41.0°	40.7° to 40.8°	40.7° to 40.8°
Tail down angle	α_{TD}	11.5°	11.1°	11.1°
Main gear spar offset	$\Delta s_{MG/RS}$	0.95 m	1.35 m	1.35 m
Main gear flap offset	$\Delta s_{Flap/SB}$	0.30 m	0.22 m	0.22 m

Funding Sources

The authors gratefully acknowledge the scientific support and HPC resources provided by the German Aerospace Center (DLR). The HPC system CARA is partially funded by "Saxon State Ministry for Economic Affairs, Labour and Transport" and "Federal Ministry for Economic Affairs and Climate Action".

Acknowledgments

The authors would like to thank Andreas Schuster and Rafael Bogenfeld from the DLR-Institute of Lightweight Systems for providing the structure model generation tool and the material properties to perform the aerostructural wing optimization presented in this publication. In addition, the authors would like to thank Lars Reimer from the DLR-Institute of Aerodynamics and Flow Technology for providing Python modules to control the fluid structure coupling and the control surface deflections in the FlowSimulator environment.

The DLR version of the AI tool DeepL was used to create the manuscript for translation tasks from German to English and vice versa.

References

[1] German Aerospace Center. *Towards zero-emission Aviation - How DLR's Aviation Research Strategy supports the European Green Deal 2050*. German Aerospace Center (DLR), Cologne, Germany, 2022. URL https://www.dlr.de/content/en/downloads/publications/brochures/2021/towards-zero-emission-aviation.html.

[2] European Commision. *Sustainable and Smart Mobility Strategy*. Office for Official Publications of the European Communities, Luxembourg, Belgium, 12 2020. ISBN 978-92-76-27370-7. doi: 10.2775/932NA-06-20-172-EN-N. URL https://ec.europa.eu/commission/presscorner/detail/en/fs_20_2350.

[3] A. Jameson, K. Leoviriyakit, and S. Shankaran. Multi-point aero-structural optimization of wings including planform variations. In *45th Aerospace Sciences Meeting and Exhibit, Reno, Nevada, USA*, number AIAA 2007-764, 2007. doi: 10.2514/6.2007-764. URL https://doi.org/10.2514/6.2007-764.

[4] J. R. R. A. Martins and J. T. Hwang. Review and unification of methods for computing derivatives of multidisciplinary computational models. *AIAA Journal*, 51(11):2582–2599, 2013. doi: 10.2514/1.J052184. URL https://doi.org/10.2514/1.J052184.

[5] G. W. K. Kenway and J. R. R. A. Martins. High-fidelity aerostructural optimization considering buffet onset. In *16th AIAA/ISSMO Multidisciplinary Analysis and Optimization Conference, Texas, USA*, 6 2015. doi: 10.2514/6.2015-2790. URL https://doi.org/10.2514/6.2015-2790.

[6] R. P. Liem, G. K. W. Kenway, and J. R. R. A. Martins. Multimission aircraft fuel-burn minimization via multipoint aerostructural optimization. *AIAA Journal*, 53(1):104–122, 2015. doi: 10.2514/1.J052940. URL https://doi.org/10.2514/1.J052940.

[7] S. Keye, T. Klimmek, M. Abu-Zurayk, M. Schulze, and Č. Ilić. Aero-structural optimization of the nasa common research model. In *18th AIAA/ISSMO Multidisciplinary Analysis and Optimization Conference*, number AIAA 2017-4145, 6 2017. doi: 10.2514/6.2017-4145. URL https://doi.org/10.2514/6.2017-4145.

[8] M. Abu-Zurayk, A. Merle, C. Ilic, S. Keye, S. Görtz, M. Schulze, T. Klimmek, C. Kaiser, D. Quero-Martin, J. Häßy, R.-G. Becker, B. Fröhler, and J. Hartmann. Sensitivity-based multifidelity multidisciplinary optimization of a powered aircraft subject to a comprehensive set of loads. In *AIAA Aviation Forum 2020*, 6 2020. doi: 10.2514/6.2020-3168. URL https://doi.org/10.2514/6.2020-3168.

[9] J. R. R. A. Martins. *Fuel Burn Reduction Through Wing Morphing*, pages 1–7. John Wiley & Sons, Ltd, 2016. ISBN 9780470686652. doi: 10.1002/9780470686652.eae1007. URL https://doi.org/10.1002/9780470686652.eae1007.

[10] J. Szodruch and R. Hilbig. Variable wing camber for transport aircraft. *Progress in Aerospace Sciences*, 25(3): 297–328, 1988. ISSN 0376-0421. doi: 10.1016/0376-0421(88)90003-6. URL https://doi.org/10.1016/0376-0421(88)90003-6.

[11] D. A. Burdette, G. K. Kenway, and J. R. R. A Maritins. Aerostructural design optimization of a continuous morphing trailing edge aircraft for improved mission performance. In *17th AIAA/ISSMO Multidisciplinary Analysis and Optimization Conference*, 2016. doi: 10.2514/6.2016-3209. URL https://arc.aiaa.org/doi/abs/10.2514/6.2016-3209.

[12] D. Reckzeh. Multifunctional wing moveables: Design of the a350xwb and the way to future concepts. In *29th Congress of the International Council of the Aeronautical Sciences, ICAS 2014*, 9 2014. URL https://www.icas.org/ICAS_ARCHIVE/ICAS2014/data/papers/2014_0298_paper.

[13] T. F. Wunderlich and F. Siebert. Optimization of control surface deflections on the high aspect ratio wing to improve cruise flight performance. In A. Dillmann, G. Heller, E. Krämer, C. Wagner, and J. Weiss, editors, *New Results in Numerical and Experimental Fluid Mechanics XIV- Contributions to the 23rd STAB/DGLR Symposium Berlin*, pages 206–215, Cham, 11 2022. Springer. doi: 10.1007/978-3-031-40482-5. URL https://doi.org/10.1007/978-3-031-40482-5.

[14] R. J. White. Improving the airplane efficiency by use of wing maneuver load alleviation. *Journal of Aircraft*, 8(10): 769–775, 1971. doi: 10.2514/3.59169. URL https://doi.org/10.2514/3.59169.

[15] G. E. Bendixen, R. F. O'Connell, and C. D. Siegert. Digital active control system for load alleviation for the lockheed l-1011. *The Aeronautical Journal*, 85(849):430–436, 1981. doi: 10.1017/S0001924000030244.

[16] C. D. Regan and C. V. Jutte. Survey of applications of active control technology for gust alleviation and new challenges for lighter-weight aircraft. Technical Report NASA/TM-2012-216008, National Aeronautics and Space Administration, 2012. URL https://ntrs.nasa.gov/citations/20120013450.

[17] R. M. Bogenfeld, S. Freund, S. Dähne, T. F. Wunderlich, and T. Wille. Damage tolerance allowable calculation for the aircraft design with static ultimate load. *Composite Structures*, 12 2023. doi: 10.1016/j.compstruct.2023.117803. URL https://doi.org/10.1016/j.compstruct.2023.117803.

[18] V. Handojo, J. Himisch, K. Bramsiepe, W. R. Krüger, and L. Tichy. Potential estimation of load alleviation and future technologies in reducing aircraft structural mass. *Aerospace*, 9(8), 2022. ISSN 2226-4310. doi: 10.3390/aerospace9080412. URL https://doi.org/10.3390/aerospace9080412.

[19] S. Binder, A. Wildschek, and R. De Breuker. The interaction between active aeroelastic control and structural tailoring in aeroservoelastic wing design. *Aerospace Science and Technology*, 110:106516, 2021. ISSN 1270-9638. doi: 10.1016/j.ast.2021.106516. URL https://doi.org/10.1016/j.ast.2021.106516.

[20] T. F. Wunderlich, S. Dähne, L. Reimer, and A. Schuster. Global aero-structural design optimization of composite wings with active manoeuvre load alleviation. *CEAS Aeronautical Journal*, 13(3):639–662, 7 2022. ISSN 1869-5590. doi: 10.1007/s13272-022-00585-3. URL https://doi.org/10.1007/s13272-022-00585-3.

[21] D. P. Raymer. *Aircraft Design: A Conceptual Approach*. AIAA education series. American Institute of Aeronautics and Astronautics, third edition edition, 1999. ISBN 978-1-56347-281-7.

[22] M. Schulze, T. Klimmek, F. Torrigiani, and T. F. Wunderlich. Aeroelastic design of the olaf reference aircraft configuration. In *Deutscher Luft- und Raumfahrtkongress (DLRK)*, 9 2021. URL https://elib.dlr.de/143642/.

[23] C. M. Liersch and M. Hepperle. A distributed toolbox for multidisciplinary preliminary aircraft design. *CEAS Aeronautical Journal*, 2(1–4):57–68, 2011. ISSN 1869-5582. doi: 10.1007/s13272-011-0024-6. URL https://doi.org/10.1007/s13272-011-0024-6.

[24] T. F. Wunderlich, S. Dähne, L. Reimer, and A. Schuster. Global aerostructural design optimization of more flexible wings for commercial aircraft. *Journal of Aircraft*, 58(6):1254–1271, 2021. doi: 10.2514/1.C036301. URL https://doi.org/10.2514/1.C036301.

[25] T. F. Wunderlich, S. Daehne, L. Reimer, A. Schuster, and O. Brodersen. Global aero-structural design optimization of more flexible wings for commercial aircraft. In *AIAA Aviation Forum 2020*, 6 2020. doi: 10.2514/6.2020-3170. URL https://doi.org/10.2514/6.2020-3170.

[26] A. B. Lambe and J. R. R. A. Martins. Extensions to the design structure matrix for the description of multidisciplinary design analysis and optimization processes. *Structural and Multidisciplinary Optimization*, 46:273–284, 2012. doi: 10.1007/s00158-012-0763-y. URL https://doi.org/10.1007/s00158-012-0763-y.

[27] A. Rempke. Netzdeformation mit elastizitätsanalogie in multidisziplinärer flowsimulator-umgebung. In *20. DGLR - Fach - Symposium der STAB 2016*, volume 2016, pages 128–129, 2016. URL https://elib.dlr.de/109263.

[28] L. Reimer, R. Heinrich, and M. Ritter. Towards higher-precision maneuver and gust loads computations of aircraft: Status of related features in the cfd-based multidisciplinary simulation environment flowsimulator. In A. Dillmann, G. Heller, E. Krämer, C. Wagner, C. Tropea, and S. Jakirlić, editors, *New Results in Numerical and Experimental Fluid Mechanics XII*, pages 597–607, Cham, 2020. Springer International Publishing. ISBN 978-3-030-25253-3. doi: 10.1007/978-3-030-25253-3_57. URL https://doi.org/10.1007/978-3-030-25253-3_57.

[29] T. Führer, C. Willberg, S. Freund, and F. Heinecke. Automated model generation and sizing of aircraft structures. *Aircraft Engineering and Aerospace Technology*, 88(2):268–276, 2016. doi: 10.1108/AEAT-02-2015-0054.R1. URL https://elib.dlr.de/103351.

[30] T. Gerhold. Overview of the hybrid rans tau-code. In N. Kroll and J. K. Fassbender, editors, *MEGAFLOW - Numerical Flow Simulation for Aircraft Design*, volume 89, pages 81–92, Berlin, Heidelberg, 2005. Springer Berlin Heidelberg. ISBN 978-3-540-32382-2. doi: 10.1007/3-540-32382-1_5. URL https://doi.org/10.1007/3-540-32382-1_5.

[31] M. Meinel and G. O. Einarsson. The flowsimulator framework for massively parallel cfd applications. In *PARA 2010 conference, 6-9 June, Reykjavik, Iceland*, 2010. URL https://elib.dlr.de/67768.

[32] S. Dähne, T. Bach, and C. Hühne. Steps to feasibility for laminar wing design in a multidisciplinary environment. In *29th Congress of the International Council of the Aeronautical Sciences, ICAS 2014*, 9 2014. URL https://elib.dlr.de/90644.

[33] H. Barnewitz and B. Stickan. Improved mesh deformation. In B. Eisfeld, H. Barnewitz, W. Fritz, and F. Thiele, editors, *Management and Minimisation of Uncertainties and Errors in Numerical Aerodynamics: Results of the German collaborative project MUNA*, volume 122, pages 219–243. Berlin, Heidelberg, 2013. ISBN 978-3-642-36185-2. doi: 10.1007/978-3-642-36185-2_9. URL https://doi.org/10.1007/978-3-642-36185-2_9.

[34] G. A. Wilke. Variable-fidelity methodology for the aerodynamic optimization of helicopter rotors. *AIAA Journal*, 57 (8):3145–3158, 2019. ISSN 0001-1452. doi: 10.2514/1.J056486. URL https://doi.org/10.2514/1.J056486.

[35] D. R. Jones, M. Schonlau, and W. J. Welch. Efficient global optimization of expensive black-box functions. *Journal of Global Optimization*, 13(4):455–492, 1998. doi: 10.1023/A:1008306431147. URL https://doi.org/10.1023/A:1008306431147.

[36] A. Forrester, A. Sobester, and A. Keane. *Engineering Design via Surrogate Modelling: A Practical Guide*. Wiley, 2008. ISBN 9780470770795. doi: 10.1002/9780470770801. URL https://doi.org/10.1002/9780470770801.

[37] Daniel G. Krige. A Statistical Approach to Some Basic Mine Valuation Problems on the Witwatersrand. *Journal of the Chemical, Metallurgical and Mining Society of South Africa*, 52(6):119–139, 12 1951. doi: 10.2307/3006914. URL http://doi.org/10.2307/3006914.

[38] T. F. Wunderlich. Multidisciplinary optimization of flexible wings with manoeuvre load reduction for highly efficient long-haul airliners. In *Deutscher Luft- und Raumfahrtkongress 2022*, 9 2022. doi: 10.25967/570055. URL https://doi.org/10.25967/570055.

[39] B. M. Kulfan and J. E. Bussoletti. Fundamental parametric geometry representations for aircraft component shapes. In *11th AIAA/ISSMO Multidisciplinary Analysis and Optimization Conference, Portsmouth, Virginia, USA*, number AIAA 2006-6948, 2006. doi: 10.2514/6.2006-6948. URL https://doi.org/10.2514/6.2006-6948.

[40] B. M. Kulfan. Universal parametric geometry representation method. *Journal of Aircraft*, 45(1):142–158, 2008. doi: 10.2514/1.29958. URL https://doi.org/10.2514/1.29958.

[41] L. A. Piegl and W. Tiller. *The NURBS Book*. Monographs in Visual Communication Series. Springer-Verlag GmbH, second edition edition, 1997. doi: 10.1007/978-3-642-5. URL https://doi.org/10.1007/978-3-642-5.

[42] N. E. Antoine and I. M. Kroo. Aircraft optimization for minimal environmental impact. *Journal of Aircraft*, 41(4): 790–797, 2004. doi: 10.2514/1.71. URL https://doi.org/10.2514/1.71.

[43] T. F. Wunderlich and S. Dähne. Multidisciplinary optimization of load adaptive wings for highly efficient long-haul airliners. In *The 9th European Congress on Computational Methods in Applied Sciences and Engineering, ECCOMAS Congress 2024*, 10 2024. doi: 10.23967/eccomas.2024.095. URL https://doi.org/10.23967/eccomas.2024.095.